

Tandem photocatalytic oxidation of Rhodamine B over surface fluorinated bismuth vanadate crystals†

Shengwei Liu, Kai Yin, Wanshu Ren, Bei Cheng and Jianguo Yu*

Received 24th May 2012, Accepted 12th July 2012

DOI: 10.1039/c2jm33337f

BiVO_4 crystals with monoclinic-phase and controllable morphologies were synthesized by NaF-mediated hydrothermal processes using $\text{Bi}(\text{NO}_3)_3$ and V_2O_5 as precursors. The NaF added as a structural controller not only affected the crystal evolution processes of BiVO_4 crystals, but also enabled the *in situ* surface fluorination of the as-synthesized BiVO_4 crystals. Interestingly, the photocatalytic oxidation reactions of RhB occurred in a stepwise manner over fluorinated BiVO_4 photocatalyst, that is, a faster de-ethylation process (conversion of RhB into rhodamine) followed by a relatively slower mineralization process, involving the destruction of the conjugated structure in rhodamine. Surface fluorination favored the RhB adsorption and hole transfer between RhB molecules and BiVO_4 photocatalyst, thus progressively enhancing the initial direct hole transfer mediated de-ethylation process. In contrast, surface fluorination exerts compromised effects on the $\cdot\text{O}_2^-$ mediated mineralization process, enhancing surface RhB adsorption *versus* retarding electron transfer from BiVO_4 photocatalyst to O_2 giving rise to $\cdot\text{O}_2^-$, and consequently, moderate surface fluorine coverage is required to balance the aforementioned conflicting effects and achieve the higher mineralization rate. The present study not only demonstrates that the photocatalytic efficiency can be modified by tuning photogenerated active species and photocatalytic reaction processes, but also provides new insights into the fluorination effects on the semiconductor photocatalysis.

1. Introduction

Semiconductor photocatalysis has great potential in the fields of solar energy conversion and environmental protection.^{1–3} It is vital to design and exploit highly efficient photocatalysts for practical applications. In the past decades, various strategies were developed to improve the photocatalytic activity, selectivity and durability.^{2–4} For example, by extending the light-response range of wide band gap semiconductors (*e.g.*, anatase TiO_2 ; *ca.* 3.2 eV) and exploiting novel visible light (400–700 nm, over 40% of the total sunlight) active photocatalysts (especially mixed oxide compounds), sunlight can be used more efficiently and the overall efficiency based on the solar radiation can be improved.^{2–4} By modulating the charge diffusion and transfer dynamics, the photoexcited holes and electrons can be well separated to restrict charge recombination, and thus the photogenerated charge carriers can be used more efficiently, favoring higher quantum efficiencies.^{2–4} Nevertheless, the photocatalytic efficiencies of

most currently available visible light active photocatalysts are still far from satisfying. In this regard, novel approaches to improve photocatalytic reactivity are highly desirable. It is expected that the photocatalytic performance can be greatly modified by controlling the photocatalytic redox reaction processes and mechanism. In fact, it has been demonstrated that tandem catalysis, involving one-pot sequential transformation of the substrate *via* two (or more) mechanistically distinct reaction processes, is effective in increasing the efficiency of chemical reactions.⁵ However, up to now, tandem photocatalysis has not well investigated yet to tune the photoinduced redox reactions.

In the past decades, bismuth vanadate (BiVO_4) has been recognized as a strong photocatalyst for water oxidation and pollutant decomposition under visible light irradiation.^{6–11} The photocatalytic performance of BiVO_4 is affected by a variety of structural characteristics. Notably, the photocatalytic properties of BiVO_4 are strongly related to its crystal phase.^{6,8} BiVO_4 mainly exists in three phases, monoclinic sheelite, tetragonal zircon and tetragonal sheelite.⁶ Normally, the photocatalytic activity of monoclinic phase is much higher than that of the other two phases.^{6,8} In addition, the surface structure of BiVO_4 plays an important role to its photocatalytic activities as the photocatalytic reactions normally take place on the surface.^{7,9} Recently, great progress was achieved in controlling the surface atomic structures of BiVO_4 and understanding the facet-dependent performance.⁹ In particular, it was indicated that BiVO_4

State Key Laboratory of Advanced Technology for Material Synthesis and Processing, Wuhan University of Technology, Luoshi Road 122#, Wuhan 430070, P. R. China. E-mail: jianguoyu@yahoo.com; Fax: +86-027-87879468; Tel: +86-027-87871029

† Electronic supplementary information (ESI) available: Fig. S1 SEM images of time-dependent morphology evolution of fluorinated BiVO_4 , Fig. S2–S4 control experiments on photocatalytic mechanism of RhB oxidation. See DOI: 10.1039/c2jm33337f

sheets with exposed {040} facets showed greatly enhanced activity in the visible-light photocatalytic degradation of organic contaminants and photocatalytic oxidation of water for O₂ generation.⁹ Rational synthesis of BiVO₄ crystals with controllable surface and phase structures by novel synthetic procedures is not only necessary to study the relations between the structures and the photocatalytic properties but also a feasible approach for developing highly visible-light-active photocatalysts. Recently, it was demonstrated that fluorination of semiconductor photocatalysts can be employed to modify significantly the bulk and surface characteristics and thus the photocatalytic processes (mechanism) and kinetics.^{4,12–18} Significantly, the *in situ* fluorination (participation of fluoride in the crystallization processes of a photocatalyst) is not only effective for surface or bulk incorporation of fluorine as the post-fluorination (exposure of pre-crystallized photocatalyst to fluorine-containing atmosphere), but is also highly flexible in controlling the crystal modification in terms of phase, size, crystallinity, shape and exposed crystal facets.⁴ Notably, intensive studies on the versatile fluorination effects were mainly focused on titania-based photocatalysts, in contrast, few efforts have been devoted to understanding the effects of fluorination on other non-TiO₂ photocatalysts.^{16–18} In this study, we investigate the effects of fluoride as an additive on the crystal evolution of BiVO₄ crystals during synthesis process and the combined effects of fluorination on the photocatalytic oxidation reactions on BiVO₄ photocatalyst. Significantly, it is demonstrated that fluoride not only favors the selective formation of monoclinic phase BiVO₄ crystals with higher crystallinity and specific crystal orientation, but also enables the surface fluorination of BiVO₄ crystals, which together contribute to the superior photocatalytic reactivity and unique tandem photocatalytic reaction process of as-obtained fluorinated BiVO₄ photocatalyst for photoinduced oxidation of Rhodamine B (RhB) molecules in aqueous solution.

2. Experimental

2.1 Synthesis

All chemicals are of analytical grade, and used as received without further purification. Fluorinated BiVO₄ crystals were prepared by a simple fluoride mediated hydrothermal process. In a typical synthesis, Bi(NO₃)₃·5H₂O and V₂O₅ with a molar ratio of 2 were dispersed into 150 mL aqueous solution of NaF under vigorous stirring. The molar ratio of F to Bi added in the synthesis system is 3. The pH value was adjusted to about 6. After stirring for another 15 min, the slurry solution was transferred into a 200 mL autoclave with a Teflon liner, which was then maintained at 180 °C for 24 h. Then, the reactor was cooled to room-temperature naturally in air. The yellow precipitate was collected and washed with distilled water for more than three times. The obtained samples are denoted as BV-F3. As control experiments, pristine BiVO₄ crystals were also synthesized without NaF by a similar procedure, the sample is denoted as BV. In addition, in order to further understand the effects of excessive NaF, fluorinated BiVO₄ crystals were also produced by a similar procedure with the designed molar ratio of F to Bi equal to 6 in the synthesis system, and the sample is denoted BV-F6. All samples were dried at 80 °C for 6 h for characterization.

2.2 Characterization

Powder X-ray diffraction (XRD) patterns were obtained on a D/Max-RB X-ray diffractometer (Rigaku, Japan) with Cu K α radiation ($\lambda = 0.15418$ nm) at a scan rate (2θ) of 0.05 s⁻¹. The accelerating voltage and the applied current were 40 kV and 80 mA, respectively. The Brunauer–Emmett–Teller (BET) specific surface areas (S_{BET}) and porous structures of the samples were analyzed by a Micromeritics ASAP 2020 nitrogen adsorption apparatus (USA). All of the samples were degassed at 180 °C before nitrogen adsorption measurements. The S_{BET} was determined by a multipoint BET method using the adsorption data in the relative pressure (P/P_0) range of 0.05–0.3. The desorption isotherm was used to determine the pore size distribution *via* the Barret–Joyner–Halender (BTH) method, assuming a cylindrical pore modal.¹⁹ Scanning electron microscopy (SEM) was performed with a JSM-5610LV microscope (JEOL, Japan) at an accelerating voltage of 20 kV. Raman spectra were recorded at room temperature using a micro-Raman spectrometer (Renishaw InVia) in the backscattering geometry with a 514.5 nm or 633 nm laser as excitation source. X-ray photoelectron spectroscopy (XPS) measurements were done with K-Alpha-surface Analysis (Thermon Scientific) using X-Ray Monochromatisation. UV-visible diffuse reflectance spectra were obtained for the dry-pressed disk samples with a UV-Visible spectrophotometer (UV-2550, Shimadzu, Japan). BaSO₄ was used as a reflectance standard in a UV-visible diffuse reflectance experiment.

2.3 Measurement of photocatalytic reactivity

The photocatalytic reactivity of the as-prepared samples was estimated by photocatalytic oxidation of Rhodamine B (RhB) aqueous solution at ambient temperature. Experimental details were as follows: 0.1 g of the sample was dispersed into a 20 mL RhB aqueous solution with a concentration of 1×10^{-5} mol L⁻¹ in a 90 mm culture dish. After dye adsorption equilibrium, a 350 W xenon lamp with a 420 nm cutoff filter positioned 25 cm above the dish was used as a visible-light source to trigger the photocatalytic reaction. The integrated visible-light intensity striking on the surface of the reaction mixture measured by using a visible-light radiometer (Model: FZ-A, China) was 75 mW cm⁻² with the wavelength range of 420–1000 nm. The concentration of RhB was monitored by a UV-2550 UV-visible spectrophotometer (Shimadzu, Japan).

3. Results

3.1 XRD results

The phase structure of BiVO₄ is of great importance for its photocatalytic activity. XRD was used to investigate the changes of phase structures of the pristine and fluorinated BiVO₄ samples. Fig. 1 shows the XRD patterns of as-prepared fluorinated *versus* pristine BiVO₄ samples. As shown in Fig. 1a, although the monoclinic phase BiVO₄ (JCPDS no. 14-0688)^{6,8,20} is dominant in the pristine BiVO₄ sample prepared without NaF, there is also a small amount of other impurity phases coexisted in the pristine BiVO₄ sample. For example, as marked with star (*) in Fig. 1a, the minor diffraction peak located at $2\theta = 24.4^\circ$ is

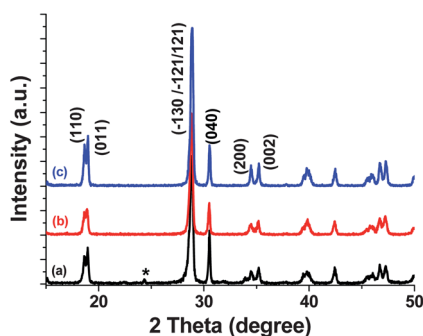
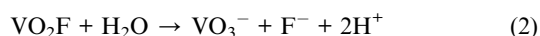


Fig. 1 XRD patterns of as-prepared fluorinated (b and c) versus pristine BiVO₄ (a) samples: (a) BV; (b) BV-F3, (c) BV-F6.

appeared, which is characteristic of tetragonal phase BiVO₄ (corresponding to the (200) face of tetragonal phase BiVO₄).^{6,8,20} The present result is consistent with previous studies using V₂O₅ as precursor.²⁰ In contrast, when NaF is added into the synthesis system, pure monoclinic phase BiVO₄ is obtained (Fig. 1(b) and (c)). Compared with the tetragonal phase, the Bi–O polyhedron in the monoclinic phase BiVO₄ is more distorted, which is supposed to be important for a higher photocatalytic activity of monoclinic phase BiVO₄.⁶ Incidentally, in our previous studies, it was also disclosed that fluoride affects the phase formation of TiO₂, favoring the selective formation of anatase-phase TiO₂ (a metastable phase of TiO₂).^{4,14} Why would NaF affect the phase formation of BiVO₄ crystals? The reaction processes in the present synthesis system with NaF can be resumed as follows:



It is known that F[−] ions can enhance the dissolution and reaction of V₂O₅ by nucleophilic substitution (eqn (1) and (2)).²¹ In this regard, the addition of NaF in the reaction system may affect the reaction processes and dynamics in the synthesis process of BiVO₄. In addition, considering that the surface Bi–OH groups on BiVO₄ crystals should be at least partially protonated giving rise to Bi–OH₂⁺ in the present synthesis system, the F[−] ions may adsorb on the surface of BiVO₄ and affect the crystal evolution by certain steric hindrance.

On the other hand, the crystal orientation of as-prepared BiVO₄ crystals is also influenced by the NaF, as evidenced by the variation in relative intensity of characteristic diffraction peaks. Typically, the relative intensity of the (040) vs. (011) peak (*I*₀₄₀/*I*₀₁₁) of monoclinic phase BiVO₄ decreases significantly for fluorinated BiVO₄ samples as compared with that for the pristine BiVO₄ sample. The *I*₀₄₀/*I*₀₁₁ are 1.46, 1.24 and 0.81 for BV, BV-F3 and BV-F6, respectively. This result suggests that added NaF facilitates the fast crystal growth of monoclinic phase BiVO₄ along [040] direction along with the promoted elimination of (040) facet.⁹

3.2 SEM images

BiVO₄ crystals with various morphologies have been synthesized by controlling the synthesis methods and experimental conditions.^{6–10,20,22,23} To investigate the effects of NaF added in the synthesis system on the morphology evolution of BiVO₄ samples, SEM images (Fig. 2) was used to characterize the BiVO₄ samples synthesized in the absence versus presence of NaF. Without NaF, backbone-like particles assembled from arrayed nanoshuttles are prepared together with some ill-shaped nanoparticles and their aggregates (Fig. 2a). Typically, those pristine BiVO₄ particles have sharp tips. Similar results were also reported elsewhere.^{20,22,23} In contrast, in the presence of NaF, the as-prepared fluorinated BiVO₄ particles are composed of larger polyhedra with well-defined facets and some underdeveloped smaller ones (Fig. 3b). The time-dependent evolution experiments of sample BV-F3 basically supported the dissolution-recrystallization mechanism, as shown in Fig. S1 (ESI[†]), amorphous BiVO₄ aggregates gradually evolved into increasingly larger BiVO₄ polyhedra. It is proposed that the NaF added in the synthesis system affects both the nucleation dynamics (reaction processes) and the surface chemistry of BiVO₄ nuclei, directing the crystal evolution and the morphological expression of the final fluorinated BiVO₄ crystals.

3.3 BET results

The porous structure and BET surface areas of fluorinated and pristine BiVO₄ crystals are investigated based on the nitrogen sorption measurement. Fig. 3 shows the nitrogen sorption isotherms for fluorinated versus pristine BiVO₄. The isotherms for both samples are of type IV (BDDT classification) with a typical hysteresis loop, associated with capillary condensation of gases within mesopores (2–50 nm).¹⁹ The specific surface areas of fluorinated and pristine BiVO₄ are 1.8 and 3.5 m² g^{−1}, respectively. A smaller specific surface area of fluorinated BiVO₄ than the pristine BiVO₄ suggests the grain growth of BiVO₄ growth is promoted by NaF. Such a result is similar to the phenomenon observed in fluoride-mediated growth of anatase TiO₂ crystals.^{4,14} The corresponding pore size distribution curves are shown in the inset of Fig. 3. Overall, the pore volume is quite small. This is not surprising taking account the micrometer scale of the BiVO₄ crystal size. The formation of pores is due to the intra-agglomeration and inter-agglomeration of the BiVO₄ particles.²⁴ As NaF facilitates the crystal growth and dispersion of BiVO₄ crystal, the intra-agglomerated pores are largely eliminated for fluorinated BiVO₄ crystals relative to the pristine ones.

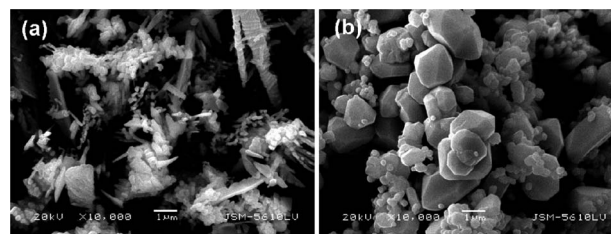


Fig. 2 SEM images of as-prepared fluorinated (b) versus pristine BiVO₄ (a) samples: (a) BV; (b) BV-F3.

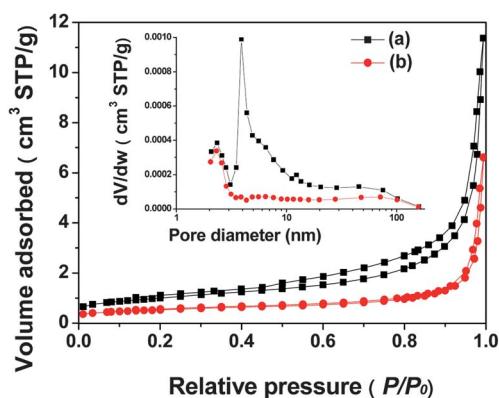


Fig. 3 N_2 sorption curves and the corresponding pore size distribution (inset) of as-prepared fluorinated (b) versus pristine $BiVO_4$ (a) samples: (a) BV; (b) BV-F3.

3.4 XPS analysis

The surface chemical states of as-prepared products are investigated using XPS. Fig. 4 shows the high resolution XPS spectra of Bi 4f, V 2p, O 1s and F 1s detected in the fluorinated $BiVO_4$ crystals (Fig. 4b) in comparison with pristine $BiVO_4$ crystals (Fig. 4a). Basically, there is no appreciable shift in the peak position for the characteristic Bi 4f_{5/2} and Bi 4f_{7/2} signals, V 2p_{1/2} and V 2p_{3/2} signals, and O 1s peak (Fig. 4), suggesting the incorporated fluorine for as-prepared fluorinated $BiVO_4$ crystals is mainly adsorbed on the surface of $BiVO_4$ crystals, which is further confirmed by the lower binding energy of F 1s (~682 eV). It was reported that the fluorine ions in the interstitial lattice of $ZnWO_4$ corresponded to the binding energy of ca. 684 eV, which is much smaller than the binding energy (688 eV) corresponding to lattice doped F in TiO_2 .¹⁸ It is not surprising that the present binding energy corresponding to adsorbed fluorine on the surface of $BiVO_4$ crystals is smaller than that reported for adsorbed fluorine on TiO_2 surface.

3.5 Raman spectra

The local structures of as-prepared fluorinated and pristine $BiVO_4$ crystals were studied by Raman spectroscopy. Raman spectra of $BiVO_4$ synthesized with and without NaF are shown in Fig. 5. Notably, the Raman spectra excited by 514.5 nm (Fig. 5A)

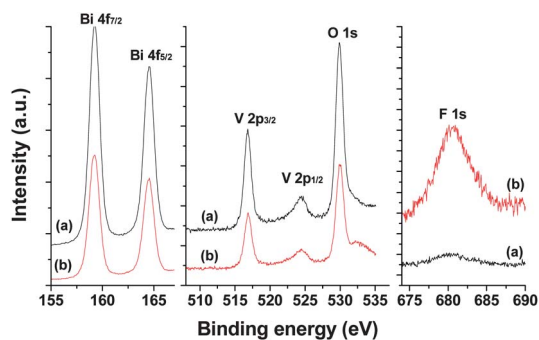


Fig. 4 High resolution XPS spectra of Bi 4f, V 2p, O 1s and F 1s detected in the as-prepared fluorinated (b) versus pristine $BiVO_4$ (a) samples: (a) BV; (b) BV-F3.

and 632.8 nm (Fig. 5B) lasers are largely different. In particular, two Raman bands located at ca. 639 and 705 cm^{-1} were detected using 632.8 nm laser in addition to the four typical Raman bands located at 209, 325, 367 and 827 cm^{-1} that were also recorded using 514.5 nm laser. These six Raman bands are all the typical vibrational bands of $BiVO_4$.^{7,23} Specifically, the 209 cm^{-1} band is related to the external mode (rotation/translation) of $BiVO_4$; the Raman bands at 325 and 367 cm^{-1} are assigned to the asymmetric and symmetric deformation modes of the VO_4^{3-} tetrahedron, respectively; the Raman band at 639 cm^{-1} was assignable to the asymmetric stretching vibration of the V–O bond; and the Raman bands at 705 and 827 cm^{-1} are attributed to the stretching modes of two different types of V–O bonds. In addition to the presence of new Raman peaks, there are also obvious variations in the peak intensities using a 632.8 nm laser instead of a 514.5 nm laser. It is well-known that the penetration depth of the 632.8 nm laser into $BiVO_4$ crystal is different from that of the 514.5 nm laser. The difference in the Raman spectra excited by the two different lasers suggests that the local structure near the surface layer is different from that in the bulk.⁷ Significantly, the peak position of Raman bands of $BiVO_4$ crystals are not affected too much by surface fluorination, further confirming that the incorporated fluorine are not entered into the lattice of $BiVO_4$ crystals. Otherwise, variations in the width and the relative intensity of those Raman bands were observed, especially when 632.8 nm laser was used as excitation light, suggesting that the surface local structures were different from each other.⁷ The fluoride induced variation in surface chemistry and crystal shape should be responsible for the aforementioned variation in Raman intensities.

3.6 UV-vis diffuse reflectance spectra

The UV-visible diffuse reflectance spectra of fluorinated and pristine $BiVO_4$ samples are shown in Fig. 6. Both samples are yellow and show strong absorption in the visible light region up to ~525 nm in addition to that in the UV light region. The steep shape of the spectrum indicates that the visible light adsorption is not due to the transition from the impurity level but to the band-gap transition.⁸ It is observed that the absorption edge for the fluorinated $BiVO_4$ samples exhibited slight red shift relative to the pristine $BiVO_4$ samples. As the incorporated fluorine are dominantly adsorbed on the surface of fluorinated $BiVO_4$

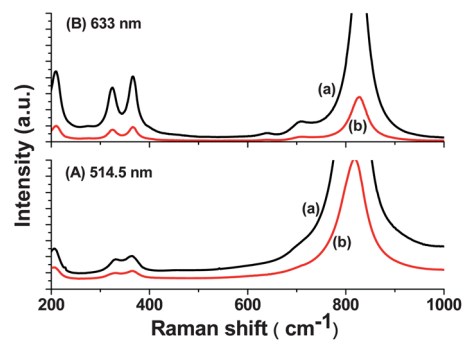


Fig. 5 Raman spectra excited by 514.5 nm (A) and 632.8 nm (B) lasers for as-prepared fluorinated (b) versus pristine $BiVO_4$ (a) samples: (a) BV; (b) BV-F3.

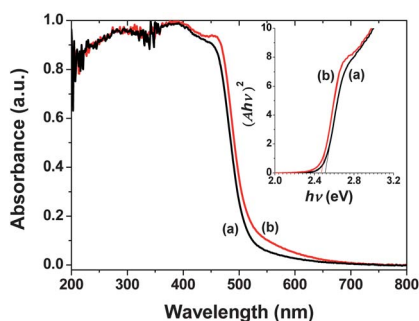


Fig. 6 Normalized UV-vis diffuse reflectance spectra of as-prepared fluorinated (b) versus pristine BiVO_4 (a) samples: (a) BV; (b) BV-F3. The inset shows the corresponding plots of $(Ah\nu)^2$ vs. $h\nu$ for the band gap energies.

crystals (XPS results), the aforementioned red-shift in absorption edge is possibly related to the phase and shape variation. The shape-dependent optical absorption of BiVO_4 crystals was previously presented by Yu *et al.*¹⁰ In addition, the phase transition of BiVO_4 crystals from tetragonal phase to monoclinic phase gives rise to narrower band gap and wider absorption band.⁶ The band gap energies for fluorinated and pristine BiVO_4 crystals, estimated from the plots of $(Ah\nu)^2$ vs. $h\nu$ (inset in Fig. 6), are 2.46 and 2.50 eV, respectively.

3.7 Photocatalytic activity

The RhB dye contains two *N*-ethyl groups at each side of the xanthene ring, which is stable in aqueous solution under visible light irradiation. In the presence of pristine or fluorinated BiVO_4 , RhB underwent pronounced photocatalytic degradation upon visible light irradiation (Fig. 7). The temporal UV-visible spectral changes of RhB aqueous solution during the photocatalytic degradation reactions over pristine and fluorinated BiVO_4 crystals are shown in Fig. 7A and B, respectively. Significantly, as for both pristine and fluorinated BiVO_4 samples, the wavelength corresponding to the maximal absorbance (λ_{max}) shifts gradually from the initial 552 nm towards shorter wavelength and finally reach at 496 nm, along with a gradual decrease in the maximal absorbance during photocatalytic reactions of the RhB solution, which are further quantitatively demonstrated in Fig. 7C. The blue shift of λ_{max} is frequently observed in oxidizing RhB using BiVO_4 and other multi-metal oxide as photocatalyst,^{8,10,25} which is associated with the stepwise removal of the *N*-ethyl group during degradation of RhB (*i.e.*, *N,N,N',N'*-tetra-ethylated rhodamine) molecule.^{10,12,13,16,17,25–27} Specifically, the characteristic λ_{max} of RhB and the de-ethylated rhodamine species are 552 nm (RhB), 539 nm (*N,N,N'*-tri-ethylated rhodamine), 522 nm (*N,N'*-di-ethylated rhodamine), 510 nm (*N*-ethylated rhodamine) and 498 nm (rhodamine), respectively.²⁶ Notably, rhodamine ($\lambda_{\text{max}} = 498$ nm) is the completely de-ethylated product of RhB, and further degradation is related to the decomposition of the conjugated structure (that is, the cleavage of the chromophoric ring) of rhodamine, accompanying with the progressive decrease in peak intensity of λ_{max} (498 nm) but without the blue shift of λ_{max} any more.

The degradation rate of RhB could be reflected either by estimating the blue shift in wavelength of maximum absorption

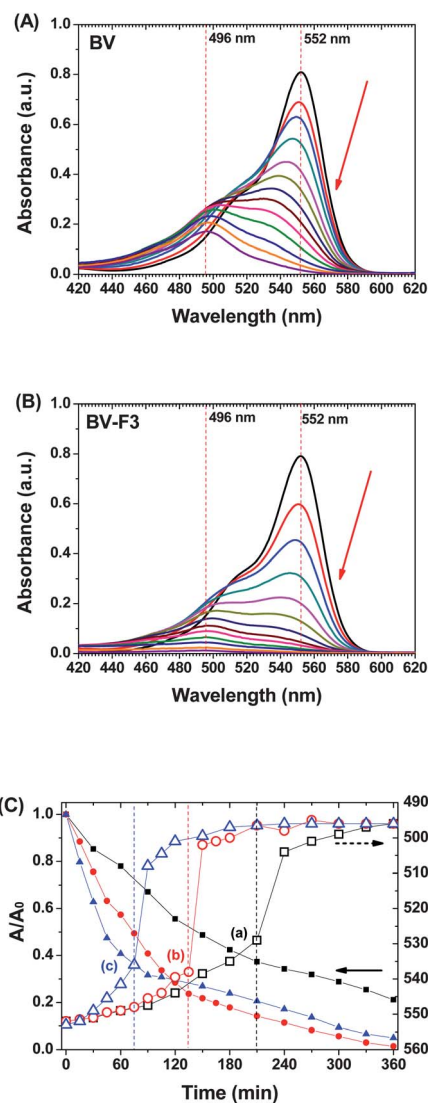


Fig. 7 (A and B) Temporal UV-visible spectral changes of RhB aqueous solution during the photocatalytic degradation reactions over pristine (A) and fluorinated (B) BiVO_4 crystals; The time interval is 30 min; (C) the change in wavelength of maximum absorption (λ_{max}) and the decrease in the maximum absorption (A/A_0) for as-prepared fluorinated (b and c) versus pristine BiVO_4 (a) samples: (a) BV, (b) BV-F3, (c) BV-F6.

(Fig. 8A) or by analyzing the temporal decrease in maximal absorbance (Fig. 8B).^{13,27} The degree of de-ethylation can be represented by the blue shift in wavelength of maximum absorption: $\Delta\lambda_{\text{max}} = 552 - \lambda_{\text{max}}$.¹³ Fig. 8A shows the degree of de-ethylation ($\Delta\lambda_{\text{max}}$) during photocatalytic oxidation of RhB on pristine or fluorinated BiVO_4 samples. Significantly, as for all BiVO_4 samples, the de-ethylation occurs dominantly in the early stage, at the end of this stage, there is a leap in $\Delta\lambda_{\text{max}}$, and then $\Delta\lambda_{\text{max}}$ is very limited (Fig. 8A), indicating that the de-ethylation process is almost terminated during the later stage. In this regard, the overall photocatalytic RhB oxidation process can be divided into two distinctive stages at the watershed. The first stage is related to the de-ethylation process of RhB, in which the λ_{max} shifts progressively from 552 nm towards 496 nm upon visible light irradiations; while the second stage is associated with the

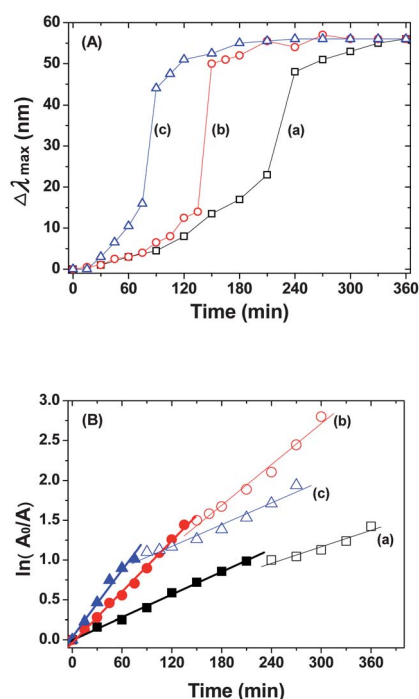


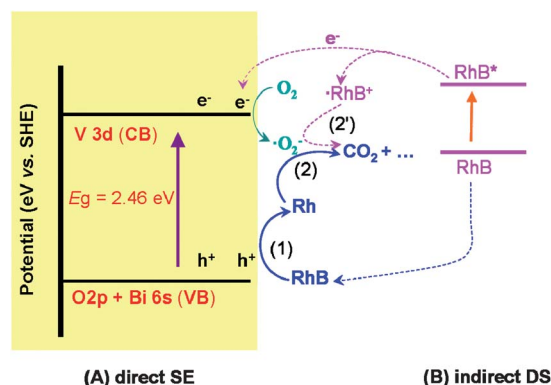
Fig. 8 (A) The degree of de-ethylation is reflected by the blue shift in wavelength of maximum absorption ($\Delta\lambda_{\max}$); (B) the two stages with different oxidation rates during photocatalytic oxidation of RhB. The rate of de-ethylation process is calculated from the temporal spectral decrease of peaks located at wavelength of 552 nm (characteristic peak of RhB), while the rate of mineralization process is calculated from the temporal spectral decrease of peaks located at wavelength of 496 nm (characteristic peak of rhodamine). The samples in A and B are corresponding to (a): BV, (b) BV-F3, (c) BV-F6.

mineralization process of rhodamine, in which the intensity of the peak centered at 496 nm decreases gradually upon further visible light irradiation, related to a decomposition of the conjugated structure of rhodamine to small molecules.¹⁶ Such a tandem two-step oxidation process of RhB is further demonstrated clearly in Fig. 8B. It is indicated that, during the photocatalytic oxidation process of RhB over all the BiVO_4 samples, there are two photocatalytic oxidation stages with different rates (Fig. 8B). Moreover, the time corresponding to the division of distinctive photocatalytic oxidation dynamics is the same as that reflected in Fig. 8A. Generally, the rate of the de-ethylation process is higher than that of the following mineralization process. In brief, the degradation of RhB over BiVO_4 samples can be separated into two consecutive but different steps, that is, a faster de-ethylation process of RhB followed by a relatively slower mineralization process of rhodamine. Admittedly, during initial dominant de-ethylation process of RhB, the slow mineralization process of rhodamine shall also occur competitively. Provided that the conjugated ring structure is not destroyed, the peak intensity at λ_{\max} for the completely de-ethylated rhodamine species should be *ca.* 70% of that for RhB (fully tetra-ethylated rhodamine species), due to their different molar extinction coefficients.²⁶ In fact, the peak intensity at 498 nm at the end of the aforementioned de-ethylation process is 40–50% of the initial peak intensity at 552 nm (Fig. 7).

The surface fluorination exerts considerable influence on both the de-ethylation process and the following mineralization process. The reaction time required for the completion of the de-ethylation process is greatly reduced upon surface fluorination (Fig. 8A), which is consistent with the higher rate of the de-ethylation process for the fluorinated BiVO_4 samples (Fig. 8B). Moreover, it seems that fluorinated BiVO_4 samples synthesized with higher NaF dosage result in higher rate of de-ethylation process. The positive effects of surface fluorination on the photocatalytic de-ethylation process of RhB molecules were also reported using other fluorinated photocatalysts.^{4,13,16} On the other hand, the effects of fluorination on the mineralization process are nonlinearly dependent on the NaF dosage used for synthesizing fluorinated BiVO_4 samples. Fluorinated BiVO_4 sample synthesized with moderate NaF dosage (BV-F3) facilitates the mineralization process, but fluorinated BiVO_4 sample synthesized with excess NaF dosage (BV-F6) retards the mineralization process. At a glance, excess NaF in the synthesis system not only eliminates the highly active (040) facet, but also reduces the specific surface areas, which impair the photocatalytic activity.⁹

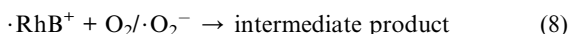
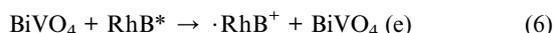
4. Discussion

It is well-established that the visible-light photocatalytic degradation of dyes in the presence of visible-light responsive semiconductor photocatalysts probably initiates through two distinctive photochemical pathways, namely, direct semiconductor excitation (SE) and indirect dye sensitization (DS).^{25,26} BiVO_4 is able to absorb visible light up to 525 nm (Fig. 6), which is attributed to the transition of the electrons from the VB (the hybrid orbitals of O 2p and Bi 6s) to the CB (the V 3d orbital) of the BiVO_4 photocatalyst (Scheme 1).^{2,6,25} In this regard, direct SE-initiated photocatalytic reactions shall take place over BiVO_4 photocatalyst under visible-light irradiation. Moreover, it is indicated that the photocatalytic mechanism for as-synthesized BiVO_4 photocatalyst is basically the same under light irradiation when excitation wavelength is within the light response range of 200–500 nm (Fig. S2†). In fact, it has been reported that BiVO_4 showed high visible light activity for photocatalytic O_2 evolution



Scheme 1 The possible pathways of the photocatalytic oxidation of RhB over fluorinated BiVO_4 photocatalysts: (A) direct semiconductor excitation (SE), and (B) indirect dye sensitization (DS). Rh denotes rhodamine, which is the completely de-ethylated product of RhB (that is, N,N,N',N' -tetra-ethylated rhodamine) molecule.

and could also be used as active visible light photocatalyst in degrading colorless organic pollutant, *e.g.*, phenol, under visible light irradiation.^{6–11} Therefore, it is reasonable that BiVO₄ is a visible light active photocatalyst for direct SE-initiated photocatalytic oxidation removal of dye pollutant RhB. The direct SE-initiated photocatalytic oxidation of organic compounds RhB over BiVO₄ photocatalyst mainly involves the following three processes (Scheme 1):²⁵ (1) the light absorption of the BiVO₄ photocatalyst and the generation of photogenerated electron (e⁻) and hole (h⁺); (2) the bulk diffusion and surface transfer of e⁻ and h⁺, and (3) surface oxidation reactions mediated by the h⁺ or their derivative active species ($\cdot\text{O}_2^-$). Notably, the $\cdot\text{OH}$ radicals is not the main active species triggering the photochemical processes over Bi-containing oxides, including BiVO₄.²⁵ This is understandable taking account of the inferior oxidation ability of photogenerated holes in VB level (a hybridization of the Bi 6s and O 2p levels) of Bi-containing oxides (Bi₂O₄/BiO⁺, +1.59 eV, *vs.* SHE), relative to the redox potential of forming $\cdot\text{OH}$ radicals ($\cdot\text{OH}/\text{OH}^-$, +1.99 eV, *vs.* SHE).²⁵ This is supported by the control experiments using different scavengers (Fig. S3†). On the other hand, RhB dyes themselves absorb the visible light in the range of 420–600 nm (Fig. 7). In particular, RhB was the main species absorbing light when irradiation wavelength $\lambda > 525$ nm. Therefore, when $\lambda > 525$ nm, the RhB photodegradation should be mainly attributed to the indirect DS-initiated photocatalytic oxidation mechanism. The indirect DS-initiated photocatalytic oxidation of dye pollutant RhB over BiVO₄ photocatalyst mainly involves the following four processes (Scheme 1):²⁵ (1) upon visible light irradiation, the photogenerated electrons were transferred to the excited state (RhB*) of the RhB dye owing to the intramolecular $\pi-\pi^*$ transition (eqn (5)); (2) the photogenerated electrons of RhB* were immediately injected into the CB (V 3d level) of BiVO₄, leaving RhB dye cation radicals ($\cdot\text{RhB}^+$) (eqn (6)); (3) the photogenerated electrons in the CB of BiVO₄ were then captured by O₂, giving rise to active species $\cdot\text{O}_2^-$ (eqn (7)); and (4) the succeeding reactions between RhB dye cation radicals $\cdot\text{RhB}^+$ and active species $\cdot\text{O}_2^-$ can lead to the oxidation of the dyes (eqn (8)). Typically, in these indirect DS-initiated processes, degradation of dyes does not involve any VB hole. The aforementioned indirect DS-initiated processes can be resumed as follows:



Overall, both the direct SE-initiated processes and the indirect DS-initiated processes would work concurrently in the present study (Scheme 1). In the present case, as indicated in Fig. S4†, the efficiency for indirect DS-initiated process is very low, which is normal due to much slower interfacial electron transfer from RhB* to CB of BiVO₄, and the direct SE-initiated processes are the predominant mechanism accounting for the RhB photodegradation.

As mentioned earlier, the hybridization of the Bi 6s and O 2p levels reduce the oxidizing power of h⁺ in VB of BiVO₄ photocatalyst to excite the production of active species $\cdot\text{OH}$ radicals. The failed production of $\cdot\text{OH}$ radicals with strong oxidizing power over BiVO₄ photocatalyst upon visible-light irradiation may be responsible for the tandem photocatalytic processes observed in the present study (Fig. 7 and 8). Normally, the direct hole transfer mediated anoxic oxidation can only destroy the chromophoric structure of the RhB, but the complete dye mineralization cannot be achieved,¹⁵ as a result, de-ethylated intermediates (denoted as Rh in Scheme 1) are produced at the first stage. Recently, Hu *et al.* also pointed out that the direct hole transfer mediated oxidation leads to the de-ethylation of RhB.¹⁶ In this regard, the major active species responsible for the mineralization of RhB is the $\cdot\text{O}_2^-$ radical (Fig. S3†).¹⁶ As mentioned above, the $\cdot\text{O}_2^-$ could be produced *via* both direct SE-initiated processes and the indirect DS-initiated processes (Scheme 1).²⁵ On the one hand, RhB (as a photo-sensitizer) is excited by visible light; the excited dye then injects an electron into the CB of the BiVO₄ *via* electron transfer to generate a conduction electron that is scavenged by the adsorbed O₂ on the surface of BiVO₄ to form $\cdot\text{O}_2^-$. On the other hand, when BiVO₄ absorbs light, the formation of $\cdot\text{O}_2^-$ could be achieved by the photogenerated electron reacting directly with O₂ adsorbed on the surface of the BiVO₄. Consequently, the mineralization processes of RhB are possibly proceeded *via* two different pathways (see reaction (2) and (2') in Scheme 1). Unfortunately, the formation rate of $\cdot\text{O}_2^-$ is normally much slower than the production of $\cdot\text{OH}$ radicals,¹ and worse, the mobility and oxidation ability of $\cdot\text{O}_2^-$ is supposed to be weaker than $\cdot\text{OH}$ radicals, which together lead to the slower mineralization process of RhB. As a consequence, the de-ethylation and mineralization process of RhB can be well separated, especially when de-ethylation process (see reaction (1) in Scheme 1) can be selectively enhanced as observed in the present study using fluorinated BiVO₄ photocatalyst. The question is whether tandem photocatalysis is advantageous over traditional photocatalysis? In the present study, the oxidation reactions of RhB occurring over fluorinated BiVO₄ photocatalyst are a typical tandem photocatalytic reactions, and shows superior photocatalytic efficiency especially when fluorinated BiVO₄ photocatalyst is synthesized with moderate NaF dosage. A stepwise reaction mode in tandem photocatalysis, involving direct hole transfer mediated anoxic oxidation (de-ethylation process) and the following indirect electron transfer (that is, electron-derived $\cdot\text{O}_2^-$) mediated oxo oxidation (mineralization process), possibly retards the back reactions and the charge recombination. It is expected that the photogenerated h⁺ and e⁻ separately take part in the tandem photochemical redox reactions not only in different reaction times (h⁺ prior to e⁻) but also in different reaction sites (terminal O-sites *versus* terminal Ti-sites), and thus can be used more efficiently.

Why would fluoride affect both the de-ethylation and the mineralization process of RhB so much? This is because the surface fluorination influences both the dye adsorption and the interfacial charge transfer. On the one hand, surface fluorination affects not only the adsorption capacity, but also significantly affects the adsorption sites and modes of molecules.⁴ Surface fluorination shall reduce the surface charges of BiVO₄ photocatalysts and favors the surface adsorption of positively

charged RhB molecules, which has been well demonstrated in studying surface fluorination of the most semiconductor photocatalysts.^{4,12,13,16} In addition, both the working functional group and the interaction force driving the adsorption of RhB on BiVO₄ may be varied after surface fluorination,¹² it was supposed that RhB was preferentially anchored on pure BiVO₄ through the carboxylic (–COOH) group, while its attachment was switched to the cationic moiety (–NEt₂ group) on the surface fluorinated BiVO₄. The enhanced RhB adsorption capacity and intensity, not only facilitated the direct SE-initiated photocatalytic oxidation of RhB *via* direct hole transfer-mediated anoxic oxidation, but also favored the indirect DS-initiated oxidation of RhB *via* electron-ejection for excited RhB to CB of fluorinated BiVO₄. This is understandable, because the efficient interfacial charge transfer between the RhB molecule and BiVO₄ photocatalyst in both processes necessitates the intimate contact between them. On the other hand, due to surface fluorination, surface electron storage is enhanced and the charge recombination is inhibited, which results in opposite influence on the hole *versus* electron transfer dynamics.⁴ As for the hole transfer, the enhanced surface electron storage and inhibited charge recombination is beneficial for the charge separation and prolonged lifetime of hole, consequently, the hole transfer is enhanced and thus the direct hole transfer mediated de-ethylation of RhB is promoted. In contrast, the enhanced surface electron storage restricted the interfacial electron transfer to O₂ giving rise to ·O₂[–], and consequently, the ·O₂[–] mediated mineralization process is somewhat retarded. Overall, the surface fluorination effects are positive for the photocatalytic de-ethylation process. In contrast, the surface fluorination effects on the ·O₂[–] mediated mineralization process are dependent on the surface fluorine coverage. Positively, the surface fluorination favors the surface RhB adsorption and electron-ejection for excited RhB to CB of fluorinated BiVO₄, being beneficial for the ·O₂[–] production. Negatively, surface fluorination enhances the surface electron storage, restricting the interfacial electron transfer to O₂ giving rise to ·O₂[–]. In this regard, the optimal moderate surface fluorine coverage shall be required to balance the conflicting effects of surface fluorination effects on the ·O₂[–] mediated mineralization process.

It should also be pointed out that, in addition to the factors mentioned above, fluorination may have a complex influence on the surface properties of synthesized BiVO₄ crystals, such as the flat-band potential, the specific surface area, and the exposed facets. These factors can in turn influence the adsorption properties and the charge transfer dynamics, and thus the photocatalytic properties. For example, the added NaF in the synthesis system affects the crystallization process of BiVO₄ crystals, eliminating the highly photoactive (040) facets with excess NaF, which may be another factor accounting for the retarded mineralization process of RhB. All those factors need further investigations.

5. Conclusions

Monoclinic-phase BiVO₄ crystals with controllable morphologies were synthesized by NaF-mediated hydrothermal processes using Bi(NO₃)₃ and V₂O₅ as precursors. The NaF added as a structural controller not only facilitated the crystal evolution of

BiVO₄ crystals with higher degree of crystallinity, lower specific surface area, and less exposed (040) facets, but also enabled the *in situ* surface fluorination the as-synthesized BiVO₄ crystals. Interestingly, the photocatalytic oxidation reactions of RhB occurring over fluorinated BiVO₄ photocatalyst is a typical tandem photocatalytic reaction, that is, a faster direct hole transfer mediated de-ethylation process and a subsequent relatively slower ·O₂[–] mediated mineralization process. Surface fluorination favored RhB adsorption and the hole transfer between RhB molecules and BiVO₄ photocatalyst, thus progressively enhancing the initial direct hole transfer mediated de-ethylation process. In contrast, surface fluorination exerts compromised effects on the ·O₂[–] mediated mineralization process, enhancing surface RhB adsorption *versus* retarding electron transfer from BiVO₄ photocatalyst to O₂ giving rise to ·O₂[–], and consequently, moderate surface fluorine coverage shall be required to balance the aforementioned conflicting effects and achieve the higher mineralization rate. The present tandem photocatalytic processes are possibly with higher efficiency over the conventional photocatalytic processes, which shall inspire new ideas in designing highly efficient photocatalysts and shall be worthy of further investigation.

Acknowledgements

This work was partially supported by the 863 Program (2012AA062701), NSFC (51072154 and 21103131) and Natural Science Foundation of Hubei Province (2010CDA078 and 2010CDB00607). Also, this work was financially supported by the Fundamental Research Funds for the Central Universities (2011-IV-034) and Self-determined and Innovative Research Funds of SKLWUT.

Notes and references

- (a) M. R. Hoffmann, S. T. Martin, W. Choi and D. W. Bahnemann, *Chem. Rev.*, 1995, **95**, 69; (b) S. Liu, J. Yu and M. Jaroniec, *J. Am. Chem. Soc.*, 2010, **132**, 11914; (c) J. Yu, G. Dai, Q. Xiang and M. Jaroniec, *J. Mater. Chem.*, 2011, **21**, 1049.
- (a) A. Kudo and Y. Miseki, *Chem. Soc. Rev.*, 2009, **38**, 253; (b) Q. Xiang, J. Yu and M. Jaroniec, *J. Am. Chem. Soc.*, 2012, **134**, 6575; (c) J. Zhang, J. Yu, Y. Zhang, Q. Li and J. R. Gong, *Nano Lett.*, 2011, **11**, 4774; (d) Q. Li, B. Guo, J. Yu, J. Ran, B. Zhang, H. Yan and J. R. Gong, *J. Am. Chem. Soc.*, 2011, **133**, 10878; (e) J. Zhang, S. Liu, J. Yu and M. Jaroniec, *J. Mater. Chem.*, 2011, **21**, 14655.
- (a) X. L. Hu, G. S. Li and J. C. Yu, *Langmuir*, 2010, **26**, 3031; (b) S. Girish Kumar and L. Gomathi Devi, *J. Phys. Chem. A*, 2011, **115**, 13211; (c) G. Liu, L. Wang, H. Yang, H. Cheng and G. Lu, *J. Mater. Chem.*, 2010, **20**, 831; (d) S. Liu, J. Yu and M. Jaroniec, *Chem. Mater.*, 2011, **23**, 4085; (e) Q. Xiang, J. Yu and M. Jaroniec, *Chem. Soc. Rev.*, 2012, **41**, 782.
- S. Liu, J. Yu, B. Cheng and M. Jaroniec, *Adv. Colloid Interface Sci.*, 2012, **173**, 35.
- (a) J. C. Wasilke, S. J. Obrey, R. T. Baker and G. C. Bazan, *Chem. Rev.*, 2005, **105**, 1001; (b) D. E. Fogg and E. N. dos Santos, *Coord. Chem. Rev.*, 2004, **248**, 2365.
- (a) A. Kudo, K. Omori and H. Kato, *J. Am. Chem. Soc.*, 1999, **121**, 11459; (b) S. Tokunaga, H. Kato and A. Kudo, *Chem. Mater.*, 2001, **13**, 4624.
- J. Yu and A. Kudo, *Adv. Funct. Mater.*, 2006, **16**, 2163.
- (a) L. Zhou, W. Wang, L. Zhang, H. Xu and W. Zhu, *J. Phys. Chem. C*, 2007, **111**, 13659; (b) L. Zhou, W. Wang, S. Liu, L. Zhang, H. Xu and W. Zhu, *J. Mol. Catal. A: Chem.*, 2006, **252**, 120.
- (a) L. Zhang, D. Chen and X. Jiao, *J. Phys. Chem. B*, 2006, **110**, 2668; (b) G. Xi and J. Ye, *Chem. Commun.*, 2010, **46**, 1893; (c) D. Wang,

- H. Jiang, X. Zong, Q. Xu, Y. Ma, G. Li and C. Li, *Chem.–Eur. J.*, 2011, **17**, 1275.
- 10 L. Ren, L. Ma, L. Jin, J. Wang, M. Qiu and Y. Yu, *Nanotechnology*, 2009, **20**, 405602.
- 11 (a) M. Long, W. Cai, J. Cai, B. Zhou, X. Chai and Y. Wu, *J. Phys. Chem. B*, 2006, **110**, 20211; (b) K. Sayama, A. Nomura, T. Arai, T. Sugita, R. Abe, M. Yanagida, T. Oi, Y. Iwasaki, Y. Abe and H. Sugihara, *J. Phys. Chem. B*, 2006, **110**, 11352; (c) P. Madhusudan, J. Ran, J. Zhang, J. Yu and G. Liu, *Appl. Catal., B*, 2011, **110**, 286; (d) B. Cheng, W. Wang, L. Shi, J. Zhang, J. Ran and H. Yu, *Int. J. Photoenergy*, 2012, 797968.
- 12 Q. Wang, C. Chen, D. Zhao, W. Ma and J. Zhao, *Langmuir*, 2008, **24**, 7338.
- 13 J. Kim, W. Choi and H. Park, *Res. Chem. Intermed.*, 2010, **36**, 127.
- 14 (a) J. Yu, W. Wang, B. Cheng and B.-L. Su, *J. Phys. Chem. C*, 2009, **113**, 6743; (b) J. C. Yu, J. Yu, W. Ho, Z. Jiang and L. Zhang, *Chem. Mater.*, 2002, **14**, 3808; (c) K. Lv, B. Cheng, J. Yu and G. Liu, *Phys. Chem. Chem. Phys.*, 2012, **14**, 5349.
- 15 (a) J. Kim, J. Lee and W. Choi, *Chem. Commun.*, 2008, 756; (b) J. Kim and W. Choi, *Energy Environ. Sci.*, 2010, **3**, 1042.
- 16 S. Hu, J. Zhu, L. Wu, X. Wang, P. Liu, Y. Zhang and Z. Li, *J. Phys. Chem. C*, 2011, **115**, 460.
- 17 H. Fu, S. Zhang, T. Xu, Y. Zhu and J. Chen, *Environ. Sci. Technol.*, 2008, **42**, 2085.
- 18 G. Huang and Y. Zhu, *J. Phys. Chem. C*, 2007, **111**, 11952.
- 19 (a) K. S. W. Sing, D. H. Everett, R. A. W. Haul, L. Moscou, R. A. Pierotti, J. Rouquerol and T. Siemieniewska, *Pure Appl. Chem.*, 1985, **57**, 603; (b) S. J. Gregg and K. S. W. Sing, *Adsorption. Surface Area and Porosity*, Academic Press, London, 1982.
- 20 J. Liu, H. Wang, S. Wang and H. Yan, *Mater. Sci. Eng., B*, 2003, **104**, 36.
- 21 J. Yu, J. C. Yu, W. Ho, L. Wu and X. Wang, *J. Am. Chem. Soc.*, 2004, **126**, 3422.
- 22 L. Zhou, W. Wang and H. Xu, *Cryst. Growth Des.*, 2008, **8**, 728.
- 23 X. Meng, L. Zhang, H. Dai, Z. Zhao, R. Zhang and Y. Liu, *Mater. Chem. Phys.*, 2011, **125**, 59.
- 24 (a) S. Liu, J. Yu and S. Mann, *J. Phys. Chem. C*, 2009, **113**, 10712; (b) S. Liu, J. Yu and S. Mann, *Nanotechnology*, 2009, **20**, 325606.
- 25 H. Fu, C. Pan, W. Yao and Y. Zhu, *J. Phys. Chem. B*, 2005, **109**, 22432.
- 26 T. Wu, G. Liu, J. Zhao, H. Hidaka and N. Serpone, *J. Phys. Chem. B*, 1998, **102**, 5845.
- 27 L. Pan, J. Zou, X. Zhang and L. Wang, *J. Am. Chem. Soc.*, 2011, **133**, 10000.